Hindawi
Advances in Civil Engineering
Volume 2022, Article ID 4915820, 10 pages
https://doi.org/10.1155/2022/4915820

Research Article

Stability Analysis of Jointed Rock Cutting Slope Based on Discrete Element Method

Wei Zhu,[1] Liang Gao,[1] Yingai Zhao,[1] Chao Yang,[2] Wei Sun,[3] and Pengqiang Yu[3]

[1]*PowerChina Roadbridge Group Co., Ltd., Beijing 100044, China*
[2]*PowerChina Zhongnan Engineering Corporation Limited, Changsha, Hunan 410014, China*
[3]*University of Science and Technology Beijing, Beijing 100083, China*

Correspondence should be addressed to Pengqiang Yu; yu_pengqiang@163.com

Received 18 May 2022; Accepted 29 June 2022; Published 16 July 2022

Academic Editor: Ziyu Tao

The joints in the rock mass are essential for the stability of rocky slopes, and the destabilization damage of the slope is often directly related to the joints. In this study, in order to reveal the instability process and mechanism of rock slopes from a microscale perspective, the DEM simulations for rocky slopes of the K88 + 400~K88 + 540 section of Zhongkai Expressway are carried out considering the influence of joints. Based on the findings of the on-site jointed structural surfaces, a rocky slope model containing two sets of intermittent joints was constructed, and the linear parallel bond model and the smooth joint model are used to characterize the rock body and joints, respectively. The evolution of microfracture, contact force chain, and particle displacement are analyzed to explore the micromechanism of slope instability. Finally, the triple reinforcement scheme of anchor cable frame and grass planting is proposed. The research results can provide a reference for stability analysis and reinforcement of similar rocky slope projects.

1. Introduction

The deformation and failure of geotechnical materials has always been a key topic [1–6]. Especially, the deformation and failure of jointed rock slope is often caused by the development of joint fissures and the destruction of structural surfaces of the rock. Under the effect of weathering and erosion for a long time, the inherent physical and mechanical properties of the slope rock with a weak layer and structural surface deteriorate; especially, the rock strength index will show obvious attenuation over time; and the microstructure inside the rock will undergo damage and accumulation, leading to macroscopic time-dependent deformation of the rocky slope with weak structural surface and finally destabilization damage of the slope. Therefore, it is particularly important to study the structural surfaces and joints of rock masses for stability analysis of rocky slopes.

Zheng and Zhao [7] adopted the finite element strength reduction method in the stability analysis of rocky slopes and obtained the sliding surface and stability coefficient of rocky slopes, which set a precedent for solving the sliding surface and safety coefficient of jointed rock slopes. Wu et al. [8] analyzed the stability of densely jointed rocky slopes using the strength reduction method based on the ubiquitous-joint model, and the results showed that the potential failure surface occurred first in the weak rock mass or along the jointing surface or both at the same time. Zhong and Miao [9] investigated the relationship between the slope safety factor and sliding mode and the sequestration of the weak interlayer within the slope using the limit equilibrium method. Based on the elastoplastic constitutive model considering complex stress state, the stability of slopes with seepage flow is analyzed using FLAC [10]. According to the field investigation and Google Earth images, Hu et al. [11] analyzed the process of fracture propagation on the slope under underground mining and then investigated the failure mechanism of the slope by the numerical software RFPA3D. Taking the process of excavation of the open-pit mine as the background, Wang et al. [12] analyzed the slope stability factor of the end slopes

using the strength reduction method, which shows that the vertical stress and stability factor decreased with the process of excavation, while the horizontal stress initially increased and then decreased. Wang et al. [13] proposed a displacement-statistics-based discrete element method and then investigated the stability of the jointed rocky slopes by incorporating the shear strength reduction method into the proposed modeling method. Meng et al. [14] proposed a hierarchical multiscale strength reduction method with a coupled FEM and DEM approach to investigate the stability of a soil and rock mixture slope. Their research showed that the multiscale simulation approach can be used as a novel numerical tool for the analysis of slope stability of geomaterials. Zhou et al. [15] investigated the effects of discontinuous joint length, dip angle, friction angle, and cohesion on slope stability based on the theoretical mechanical model of cusp catastrophe for intermittent jointed rocky slope instability. Jiang et al. [16] studied the destabilization and collapse processes of jointed rocky slopes by means of a cohesive contact model and revealed the failure mechanism at the macroscopic level of the slope. Scholtès and Donze [17] investigated the damage mechanism of jointed rocky slopes and found that the initiating weak surface of slope instability is developed from its internal cracks. The discrete element modeling method based on displacement statistics proposed by Wang et al. [18] can be combined with the strength reduction method to analyze the stability of jointed rock slopes. Zhao et al. [19] used the granular flow method to simulate the destabilization damage process of rocky slopes and explored the influence of the distribution depth and dip angle of the weak structural surface on the damage form of the slope by presetting weak structural surfaces with different distribution forms. Victor and Tedius [20] established a numerical model considering key geological features such as joints and structural planes to simulate the stability of jointed rocky slopes affected by wedge failure mechanisms. Li et al. [21] analyzed the stability of a jointed rock slope under translational failure and toppling failure by combining the quasi-static method, multidegree of freedom of rigid block element discretization technology, mathematical programming method, and plastic limit analysis method. Song and Sun [22] measured the parameters of rock structure surface by various methods and searched for the connected structure surface with minimum shear strength so called the potential slip surface, based on the depth-learning search algorithm. Shen et al. [23] used the Sarma method combined with the optimization method to analyze the stability of the down-layer sliding and cut-layer sliding methods for a large horizontal layered rock slope in the Three Gorges reservoir area affected by the combination of soft level, joints, and lithology of the slope.

In summary, although numerous studies have been conducted on jointed rock slopes, there are relatively few studies on the micromechanism of failure of crossed intermittent jointed rock slopes. In this paper, a model of cross-sectional intermittent jointed rock mass and rock slope is constructed based on the discrete element method, and the evolution law of fracture and the micromechanism of slope failure are then studied at the microscale level, which can improve the understanding of the failure mechanism of rock masses and slopes.

2. Microfracture and Joint Surface in Rock

There are many random microfractures in the rock mass, and the crack tip is prone to cause high-stress concentration under loading. When the maximum stress near the crack tip reaches the material strength value, the crack will expand unsteadily, which leads to the brittle fracture of the rock mass. Cracks generated in rock masses under load can be mainly classified as wing crack and secondary crack. The wing crack arises at the end of primary joints and gradually expands under load. It is considered by Lajtai [24] and Bobet and Einstein [25] as a type of tensile crack that starts from the crack tip and expands along the direction of maximum load. Secondary crack, on the other hand, is the shear crack that is approximately coplanar with the crack. Secondary cracks usually propagate as shear cracks in the same plane, which also arise at the end of the fracture and are the main contributors to rock damage.

The rock mass is generally composed of structural surfaces and intact rocks, which often exhibits anisotropy, nonuniformity, and discontinuity due to the complex geological processes. The structural surface is the weak surface prone to damage in the rock mass. Recently, in addition to the experimental method [26, 27], continuous constitutive modeling and discrete element method are increasingly used to simulate the deformation and failure of geotechnical materials [28–37]. The discrete element method has significant advantages in simulating cracks and large deformations. It only needs to consider the contact properties between particles and does not need to define the overall complex constitutive relationship [38–40]. The instability model of rock slopes containing joints under gravity is simulated in PFC 6.0 by synthetic rock mass, as shown in Figure 1. The synthetic rock mass is composed of a model of cohesive particles and a network of discrete fractures. The particles are connected by adhesive bonds, which make each particle glued into a whole, and under the load, the adhesive bonds are broken. For stronger rock materials, the linear parallel bonding model is often chosen as the model for bonded particles. The linear parallel bonding model can connect both particles to particles as well as to planes. Parallel bonding can provide mechanical properties stored between two contacting parts, and parallel bonding parts are similar to linear parts and establish elastic interactions. The existence of parallel bonds allows the two parts of contact to transfer force and moment to each other. The relative motion that occurs after the creation of a parallel bond results in the creation of forces and moments within the bonded material. If either of these maximum forces or moments exceed the corresponding bond strength, the parallel bond will break. Numerous joints with different orientations and trace lengths form a discrete fracture network, which is then embedded in the particle model to form a synthetic rock mass, as shown in Figure 2. The linear parallel bond model is generally used between mineral

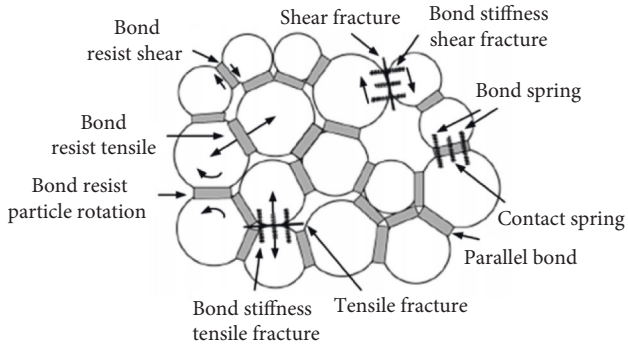

Figure 1: Linear parallel bonding model.

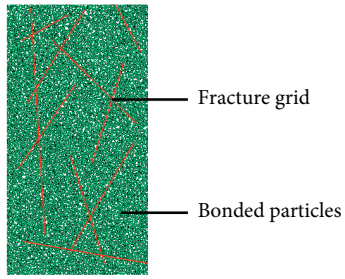

Figure 2: Synthetic rock mass map.

particles in rock, and the smooth joint model is used at the intersection of particles and fracture networks.

3. Particle Flow Model for Joint Rock Slope

A rock slope model with a width of 120 m and a height of 76 m was established and excavated in 8 stages, as shown in Figure 3. The minimum radius of particles in the model is selected as 0.15 m, and the ratio of the maximum and minimum particle sizes is equal to 2. The porosity is taken as 0.1.

According to the field investigation of Zhongkai Highway, the elastic modulus of moderately weathered granite is taken as 11 GPa, and the uniaxial compressive and tensile strengths are 28.3 MPa and 4.5 MPa, respectively. The trial-and-error method is used to calibrate the microscale parameters of moderately weathering granite used in DEM, and the main parameters of the particle model are shown in Table 1.

From the statistical results of structural surface (see Figures 4 and 5), the tendency of structural surface and slope surface is closely consistent, and there are two groups of the dominant structural surface with the dip angle of 72° and 8°, respectively.

According to the on-site investigation of the slope, the joints are mainly developed below stage 5. Hence, two groups of intermittent joints, named groups I and II, are inserted in the area below the slope of stage 5. The dip angles of the two groups of joints are 72° and 8°, respectively, and the lengths of both are 8 m, as shown in Figures 6 and 7. According to the condition of the on-site joints, the parameters of the joints can be obtained as shown in Table 2.

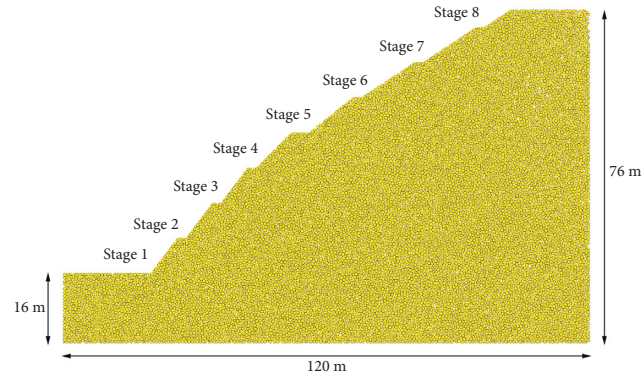

Figure 3: Particle flow model of the slope.

4. Micromechanical Analysis of the Instability of Slope

4.1. The Spatiotemporal Evolution of Microfracture in the Jointed Rock Slope. The failure mechanism of jointed rock slope in the process of instability is analyzed from the perspective of micromechanics in this section. Figure 8 shows the development of microfractures in the failure process of rock slopes controlled by two groups of bedding discontinuous joints. Microfracture was a contact fracture caused by the fact that interparticle stress exceeds its bonding strength. It can be divided into two categories according to the different fracture modes, that is, tensile fracture (denoted in red in Figure 8) and shear fracture (denoted in green in Figure 8).

It can be seen from Figure 8 that the contact fractures of the smooth joint model can be observed when the calculation reaches 1,000 time steps. Then microfractures that mainly result from tension failure are generated at the end of the joint at the state of 5,000 time steps of calculation and gradually expand to the end of the surrounding joint along the rock bridge. As shown in Figure 8, one can observe the breaking and penetration of rock bridges, such as rock bridges between the upper end of the first joint in the third layer of group I and the left end of the second joint in the second layer of group II, between the lower end of the second joint in the sixth layer of group I and the right end of the third joint in the second layer of group II, and between the upper end of the second joint in the fifth layer of group I and the right end of the second joint in the fourth layer of group II. Besides, the microfracture develops from the inside out according to the spatial position. At the state of 10,000 time steps, the crack occurs on the surface of the slope, and the internal crack continues to develop. The lower end of the second joint in the third layer of group I breaks and connects with two joints, which are the right end of the first joint in the fourth layer of group II and the left end of the first joint in the fifth layer, respectively, and rupture blocks formed on the slope surface. The rock bridge between the upper end of the three joints and the right end of the first joint in the sixth layer of group II is broken and connected, and the rock bridge between the right end of the third joint of the third layer of the group II and the left end of the third joint of the

Table 1: Model parameters of particle model.

Minimum particle radius (R_{min}/m)	Particle size ratio (R_{max}/R_{min})	Particle density, ρ (kg/m^3)	Interparticle friction coefficient, μ	Particle effective modulus, E_c (GPa)	Particle normal-to-shear stiffness ratio (kn/ks)
0.15	2	2,500	0.5	5.0	1.0
Radius multiplier, λ	Bond effective modulus, E (GPa)	Bond normal-to-shear stiffness ratio (kn/ks)	Tensile strength, pb_ten (MPa)	Cohesion, pb_coh (MPa)	Friction angle, pb_fa (°)
1	5.0	1.0	4.8	4.8	35

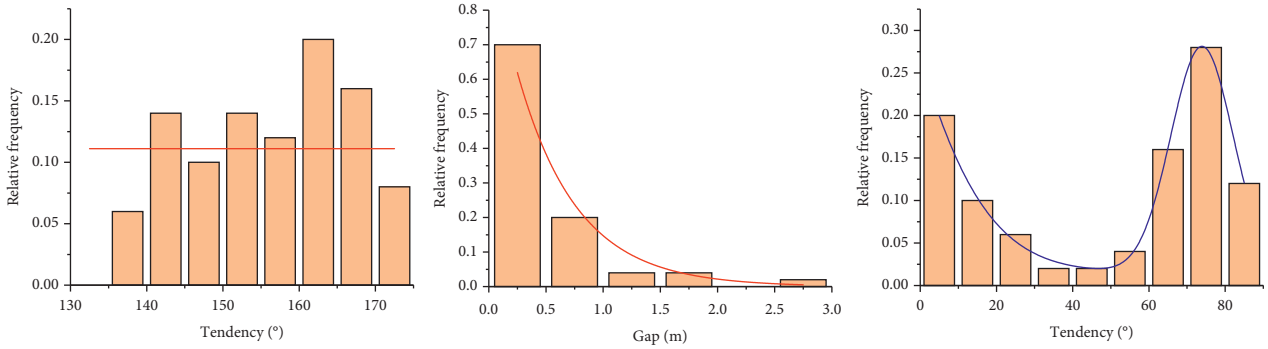

Figure 4: Histogram and probability density curve of joint tendency and dip angle.

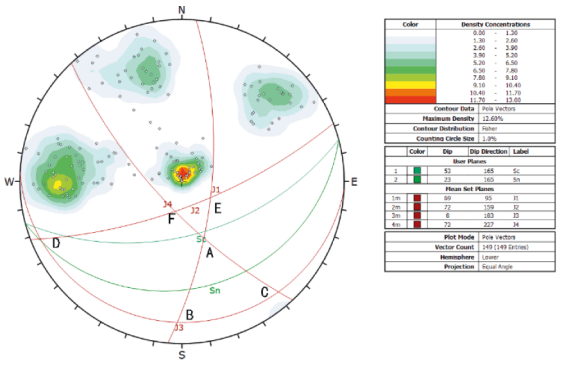

Figure 5: Isomorphic structure of joints and their poles.

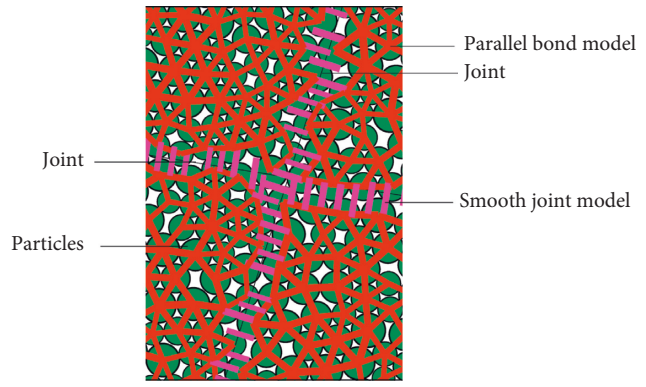

Figure 7: Discrete fracture network.

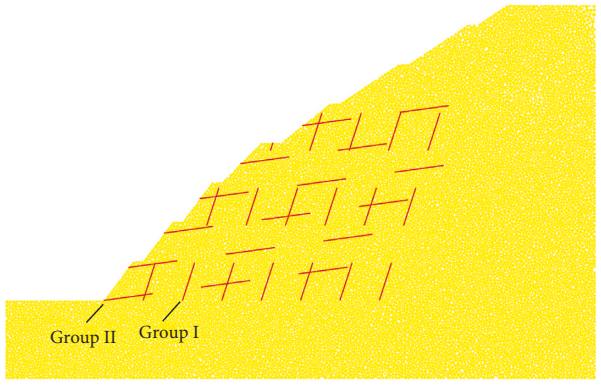

Figure 6: Discontinuous jointed rock slope model.

fourth layer of group II is broken and connected. At time step 15,000, the slope surface cracks further increase, and the right ends of the two joints in the sixth layer of group II both had ruptures with the slope surface; a macroscopic rupture zone appeared between the lower end of the third joint in the seventh layer of group I and the right end of the third joint in the fourth layer of group II. At time step 20,000, a large number of ruptures occur at the end of the first joint in the second layer of group I and the first joint in the fourth layer of group I and expand to the end of the surrounding joints; the rock bridge between the upper end of the first joint in the fifth layer of group I and the left end of the third joint in the second layer of group II broke through; and the upper end of the first joint in the sixth layer of group I develops and runs through the middle of the third joint in the second layer of group II. When the model calculates to 25,000 time steps, a large number of fissures developed in the joints at the bottom of the slope, especially at the upper end of the first joint in the second layer of group I and the left end of the third joint in the first layer of group II, and almost all of the joints have penetrating failures. Microfractures continued to occur in the fractured zones that had been penetrated in

Table 2: Main parameters of joint.

Normal stiffness (sj_kn/MPa)	Shear stiffness (si_ks/MPa)	Friction coefficient, sj_fric	Dilation angle, sj-da (°)
2×10^7	2×10^7	0.2	0
Cohesion (sj_coh/MPa)	Tensile strength (sj_ten/MPa)	Joint bond state, sj_state	Joint friction angle, sj_fa (°)
0	0	3	0

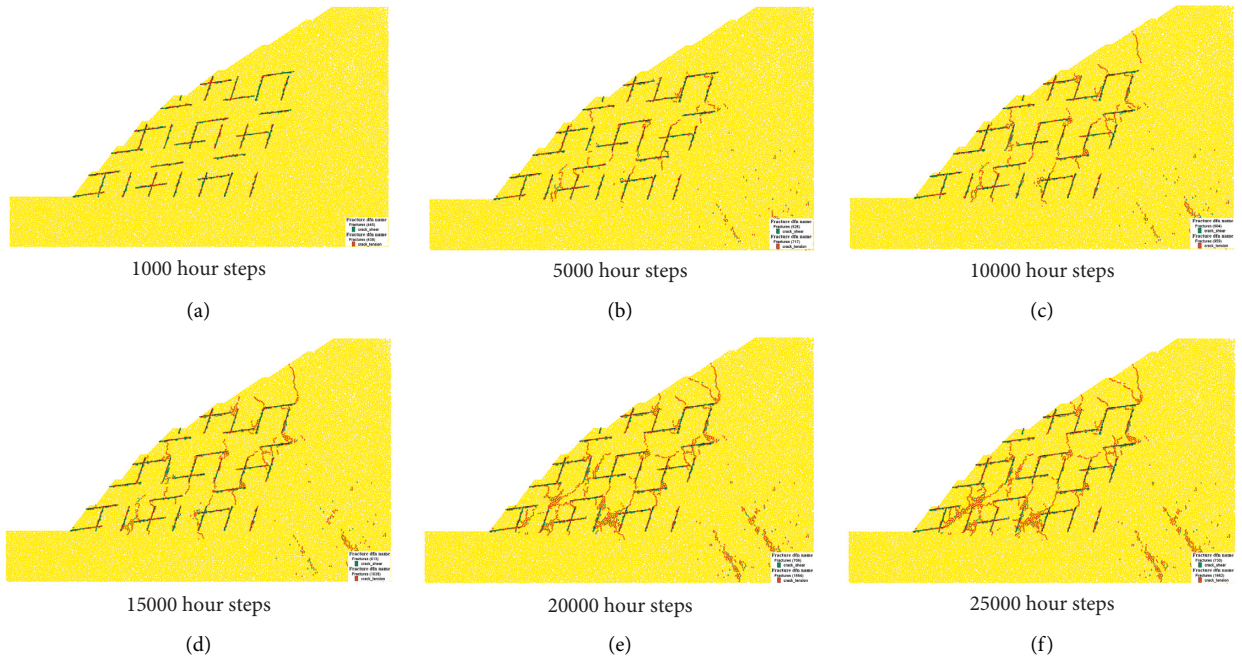

Figure 8: Mesoscale temporal and spatial development process of the rupture: (a) 1,000 hour steps, (b) 5,000 hour steps, (c) 10,000 hour steps, (d) 15,000 hour steps, (e) 20,000 hour steps, and (f) 25,000 hour steps.

many places, and the macrofracture zones were thickened and the fractures were more obvious.

As discussed above, it is found that there are two groups of layered intermittent joints (the slope angle is between the two groups of joint inclination angles) with the following failure laws: the landslide is mainly attributed to the fact that the cracks between the ends of the intermittent joints penetrate through and form a closed body separated from the parent body of the slope with the primary joints; under different time and space conditions, the microfractures are mostly tensile fractures with more vertical cracks and less transverse cracks; microcracks are preferentially generated at the joint ends of the bottom of the slope and gradually spread to the surface and upper part of the slope.

4.2. Spatiotemporal Development of Unstable and Ruptured Blocks of Jointed Rock Slopes. Figure 9 shows the time-space development process of fractured blocks, where different colors represent different fractured blocks, the fractured blocks are composed of granular bodies, and there are rock blocks separated from the rock mass due to the generation and penetration of mesofractures. The particles inside the broken block are still bound together and will continue to break into several small blocks under loading. When the model reaches 1,000 time steps, due to the rupture of smooth joints, ruptured blocks appear on the surface of the first-stage slope and the third-stage slope, in which the joints coincide with the edges of ruptured blocks, and their bottom and top are flat, and the trailing edge is steep. At the state of 5,000 time step, scattered small rupture blocks appear inside the slope, and small-area rupture blocks appear in the upper part of the first-level slope, the third-level slope, and the middle of the fifth-level slope. At 10,000 time steps, the number of scattered small fractured blocks inside continues to increase; the upper rupture block of the third-level slope continues to extend upward to the middle of the fourth-level slope; and its shape also has the characteristics of relatively gentle bottom and top and steep trailing edge. At 15,000 time steps, the scattered blocks inside the slope increase greatly, and an irregular wedge-shaped rupture block appeared from the middle of the fifth-grade slope to the middle of the seventh-grade slope on the surface; the trailing edge is steep and the bottom and left ends are flat, but the middle part is a quadrilateral embedded in the bottom. At 20,000 time steps, the internal fissures of the slope finally penetrate, and a large rupture block appears; the bottom of the large fractured block is irregular; and the trailing edge presents a steeply connected step shape. When calculation approaches 25,000 time steps, a large number of ruptured blocks appear inside,

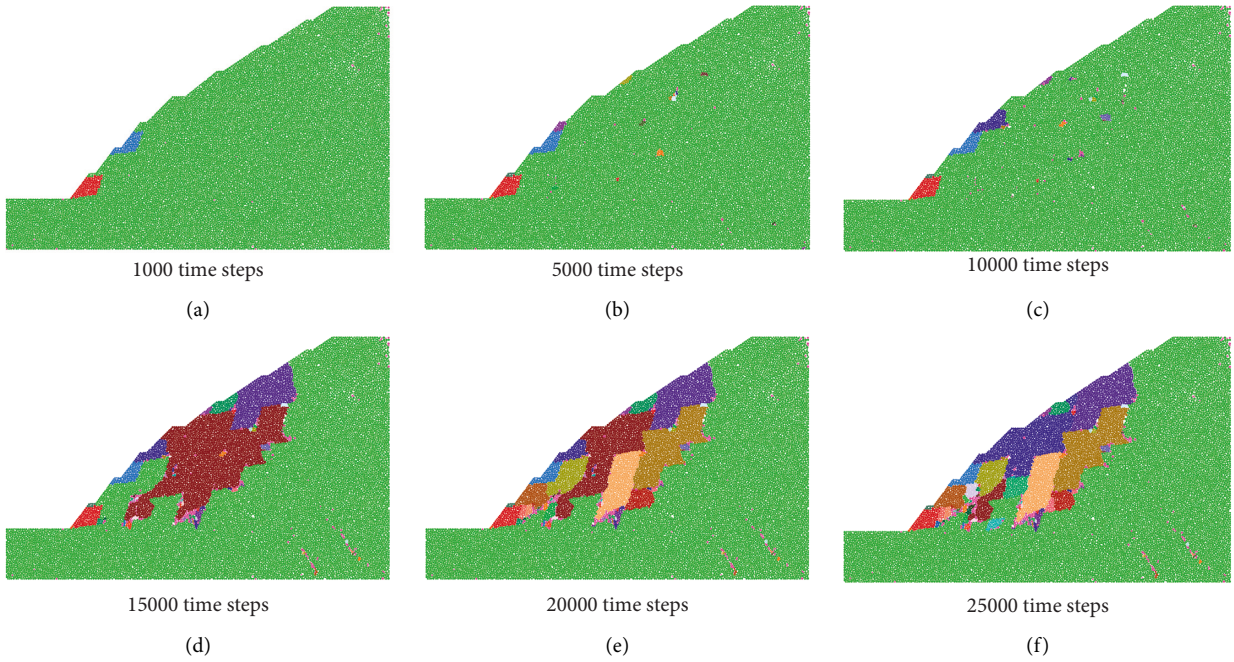

Figure 9: The spatiotemporal development process of the ruptured block: (a) 1,000 time steps, (b) 5,000 time steps, (c) 10,000 time steps, (d) 15,000 time steps, (e) 20,000 time steps, and (f) 25,000 time steps.

and on the surface of the slope, and the large inner ruptured blocks continue to rupture and divide into multiple blocks. There are ruptured blocks on the slope surface below the seventh-level slope, and most of them have the characteristics of gentle bottom and top and steep trailing edge.

Based on the analysis above, we can conclude that there are two groups of bedding discontinuous joints (the slope angle is between the two groups of joint dip angles) with the following rules when the rock slope fails: the fractured block first appeared in the lower part of the slope, then developed upward, and then occurred inside the slope; the ruptured blocks in the middle and lower parts are smaller, and the upper and inner rupture blocks are larger; most of the ruptured blocks are irregular in shape but generally show the characteristics of relatively gentle lower and upper edges and relatively steep trailing and leading edges.

4.3. Contact Force Chain and Displacement of Jointed Rock Slope. Figure 10 shows the comparison of the contact force chain before and after the instability of the jointed rock slope. As shown in Figure 10(a), the direction of the contact force on the slope surface is roughly the same as that of the slope surface. The contact force between particles inside the slope gradually recovered to the original state under the action of gravity, mainly distributing in the vertical direction and less in the horizontal direction. As shown in Figure 10(b), after the failure of the slope, the contact force between the particles at the end of the discontinuous joint is larger, which is consistent with the stress concentration phenomenon at the tip of the crack. This phenomenon is more obvious at the lower part of the slope, but near the upper and lower surfaces of the joint, the contact force is very small, and a stress arch is formed at the connection line of the rock bridge at the end of the joint, resulting in the microfracture of the slope along the end of joints.

Figure 11 shows the displacement field of particles at the end of the calculation. The displacement vector diagram of particles in Figure 11(a) directly reflects the moving direction of particles. The particles on the slope surface slide down along the slope direction, and the internal particles move downward approximately vertically. The displacement magnitude of particles is shown in Figure 11(b). The displacement of particles is larger on the slope surface and reaches a maximum of 0.4 m at the foot of the slope. However, it decreases with the location going deeper into the slope.

5. Slope Support Measures

In view that the displacement of the bottom of the slope is large and the microcracks in stages 1 to 3 of slopes are easy to be transfixed, a triple reinforcement program of anchor cable frame and grass planting is carried out. The prestressed anchor cable is combined with the reinforced concrete frame beam to form a prestressed anchor cable beam structure. In order to give full play to the antisliding ability of the landslide, the active antisliding method is adopted, and the traditional passive antisliding form is replaced by the prestressed anchor cable frame beam. The reinforcement mechanism is to transmit the anchoring force to the slope body through the interaction between the frame beam and the prestressed anchor cable, stabilize the slope surface and inside, and make the slope more stable.

According to the microscopic analysis results, the slope foot is poured with a concrete slope, and the third-level slope

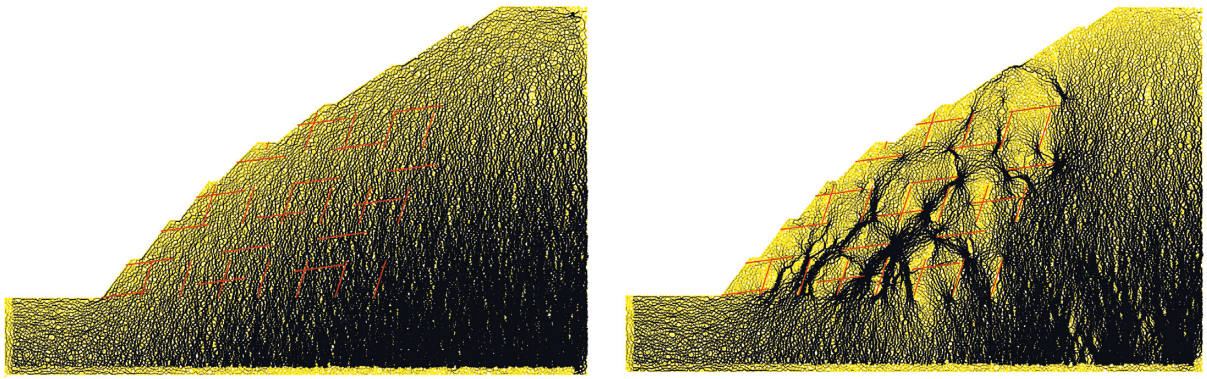

(a) (b)

Figure 10: Contact force chain diagram: (a) 0 time step and (b) 25,000 time steps.

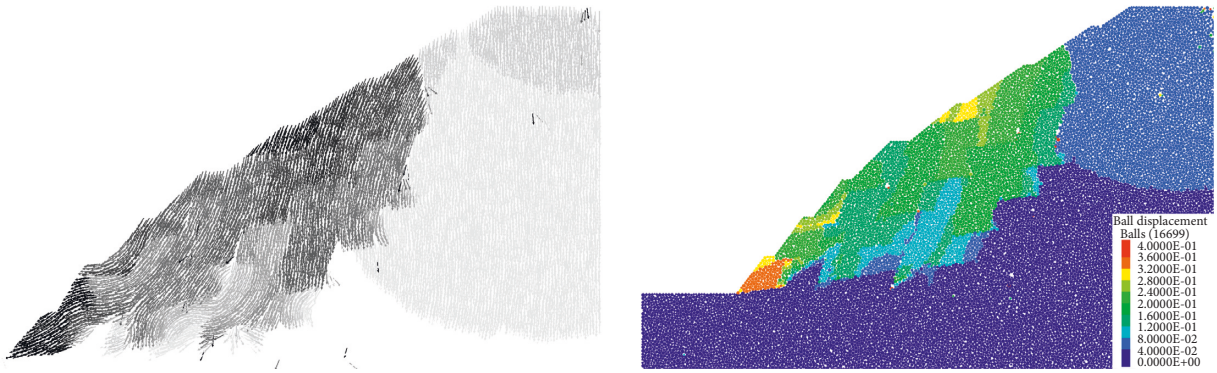

(a) (b)

Figure 11: Particle displacement diagram: (a) vector image and (b) cloud map.

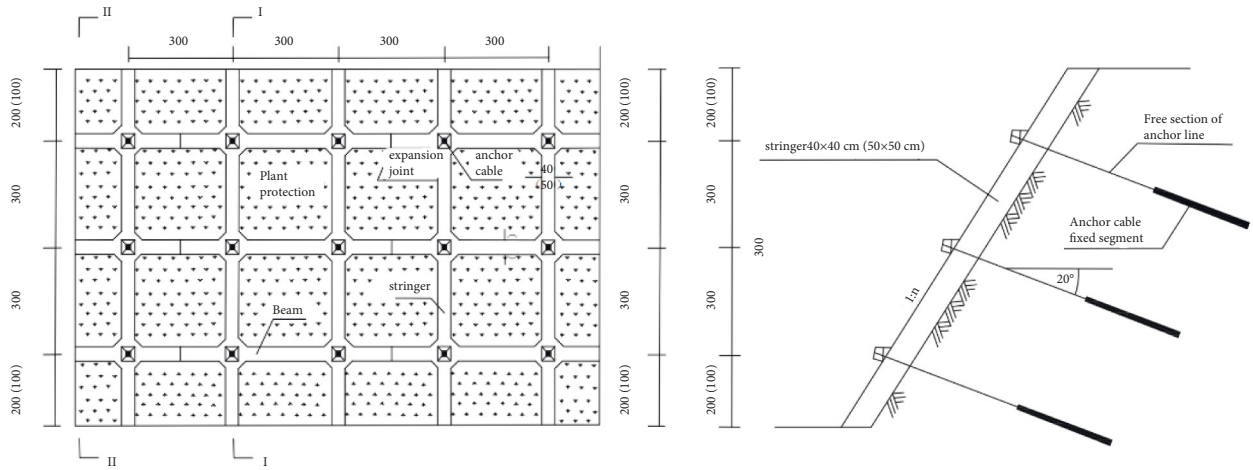

Figure 12: Construction of anchor cable frame.

uses anchor cable frame reinforcement measures. The steel strand anchors are installed by drilling holes in the slope, and the construction design of the anchor cable frame is shown in Figure 12. Three rows and six bundles of the anchor cable are adopted, of which the maximum length of the anchor cable is 20 m, the length of the anchor is 8 m with an angle of 20° with the horizontal plane, and the distance between anchor holes is 3 × 3 m. The type of six bundles of an anchor cable is OVM15-6 type, the tension strength of which is 600 kN. The reinforced concrete frame beam is set along

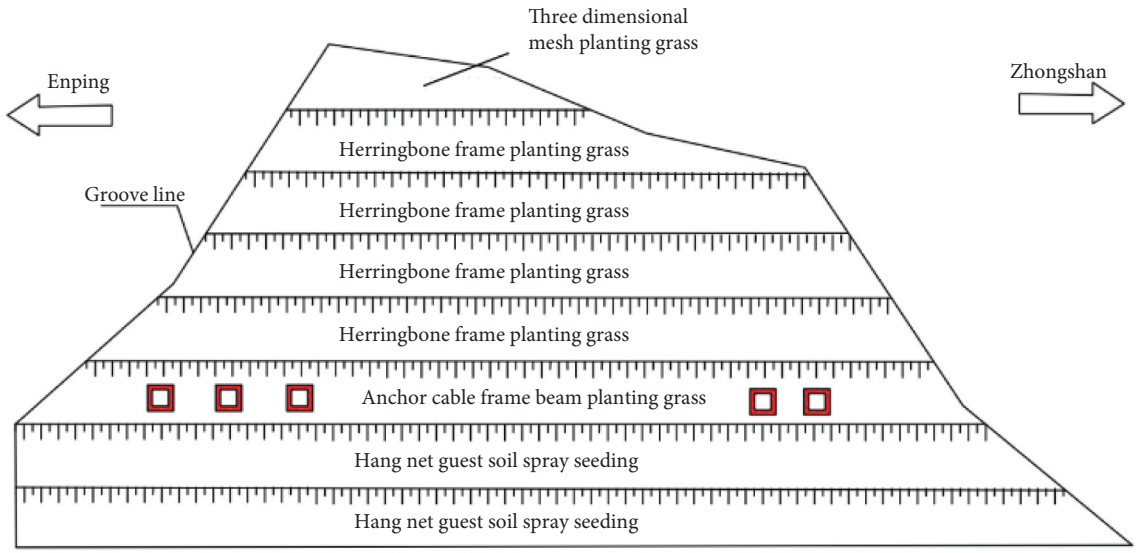

Figure 13: Schematic diagram of stress monitoring points.

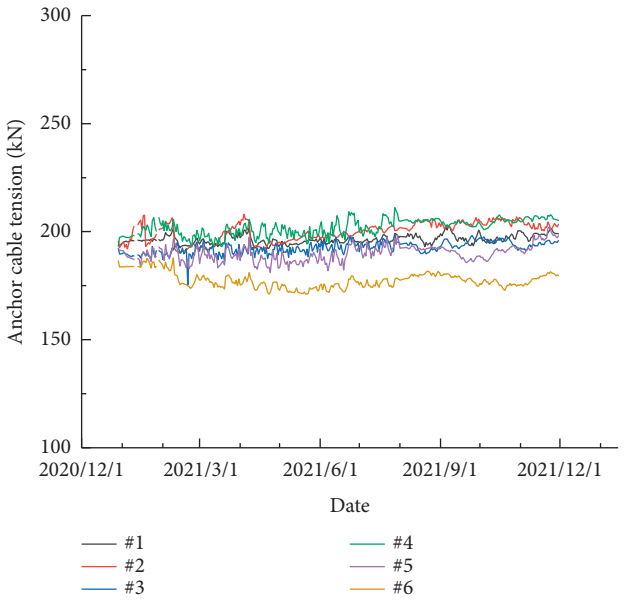

Figure 14: Stress monitoring results.

Figure 15: On-site completion situations.

the vertical and horizontal direction of the anchor hole with the rib width of 40 cm the length through the anchor hole. The frame beam is the main component of slope protection, and it is also the support point for anchor cable tensioning and anchoring. Therefore, the grass protection is made inside the frame beam, which finally constitutes the support system of the slope.

According to the anchor cable stress monitoring method, as shown in Figure 13, the anchor stress gauge is placed on the prestressed anchor cable to monitor the stress in the dangerous position shown in mesoscopic analysis (the slope of stage 3). The "real-time online display system for intelligent monitoring of high and steep road rift slopes" was developed independently to collect the monitoring data. According to the field investigations, six stress monitoring points were arranged on the slope of stage 3. The variations of stress before and after the anchor cable tensioning (see Figure 14) indicate that the reinforced slope using the above reinforcement measure is stabilized as shown in Figure 15.

6. Conclusions

In this paper a DEM model containing two groups of smooth interrupted joints of rock slopes (the slope angle is between the inclination of the two groups of joints) is constructed. The micromechanism of instability of rock slopes is analyzed from the points of microfracture, fracture block, contact force chain, and particle displacement. The detailed conclusions are as follows:

(1) The destabilization of the rocky slope is fundamentally caused by the rupture of rock intergranular adhesion, and the microfracture is mainly the result of tension failure. The microfractures firstly occur in

the internal and bottom joints of the slope and then gradually expand to the upper part of the slope with a large number of fractures in the vertical direction and fewer cracks in the horizontal direction.

(2) In the process of slope instability, the contact force at the end of the joints is large, while the contact force at the upper and lower surfaces of the joints is small, showing the phenomenon of stress arch of rock bridge.

(3) The broken particles slide down along the slope direction, and the damage is mainly located at the foot of the slope. Although a large number of cracks have occurred in the slope, there is no large-scale landslide, and the slope is generally stable. But the foot and the slope of stage 3 should be strengthened and protected.

Data Availability

The data used to support the findings of this study are available from the corresponding author upon request.

Conflicts of Interest

The authors declare that they have no conflicts of interest.

Authors' Contributions

Wei Zhu performed the data analyses and wrote the manuscript; Liang Gao established the numerical model and analyzed the results; Yingai Zhao contributed significantly to data analysis and manuscript preparation; Chao Yang and Wei Sun reviewed and edited the manuscript; Pengqiang Yu contributed to the conception and methodology of the study. All authors have read and agreed to the published version of the manuscript.

Acknowledgments

The authors gratefully acknowledge the financial support provided by PowerChina Roadbridge Group Co., Ltd. (no. LQKY2017-03).

References

[1] B. Bai, Q. Nie, Y. Zhang, X. Wang, and W. Hu, "Cotransport of heavy metals and SiO2 particles at different temperatures by seepage," *Journal of Hydrology*, vol. 597, Article ID 125771, 2021.

[2] B. Yuan, Z. Li, Z. Zhao, H. Ni, Z. Su, and Z. Li, "Experimental study of displacement field of layered soils surrounding laterally loaded pile based on transparent soil," *Journal of Soils and Sediments*, vol. 21, pp. 3072–3083, 2021.

[3] B. Bai, G. c. Yang, T. Li, and G. s. Yang, "A thermodynamic constitutive model with temperature effect based on particle rearrangement for geomaterials," *Mechanics of Materials*, vol. 139, Article ID 103180, 2019.

[4] Y. Liu and C. S. Chang, "Relationship between element-level and contact-level parameters of micromechanical and upscaled plasticity models for granular soils," *Acta Geotechnica*, vol. 15, no. 7, pp. 1779–1798, 2020.

[5] B. Bai, T. Xu, Q. Nie, and P. Li, "Temperature-driven migration of heavy metal Pb2+ along with moisture movement in unsaturated soils," *International Journal of Heat and Mass Transfer*, vol. 153, Article ID 119573, 2020.

[6] B. Yuan, Z. Li, Y. Chen et al., "Mechanical and microstructural properties of recycling granite residual soil reinforced with glass fiber and liquid-modified polyvinyl alcohol polymer," *Chemosphere*, vol. 286, Article ID 131652, 2022.

[7] Y. R. Zheng and S. Y. Zhao, "Application of strength reduction FEM in soil and rock slope," *Chinese Journal of Rock Mechanics and Engineering*, vol. 19, pp. 3381–3388, 2004.

[8] S. C. Wu, A. B. Jin, and Y. T. Gao, "Slope stability analysis by strength reduction method based on ubiquitous-joint model," *Rock and Soil Mechanics*, vol. 04, pp. 537–542, 2006.

[9] S. Zhong and Y. Miao, "Research on the influence of weak interlayer in open-pit slope on stability," *Advances in Civil Engineering*, vol. 2021, Article ID 4256740, 9 pages, 2021.

[10] Z. Ma, C. Zhu, X. Yao, and F. Dang, "Slope stability analysis under complex stress state with saturated and unsaturated seepage flow," *Geofluids*, vol. 2021, Article ID 6637098, 11 pages, 2021.

[11] Y. Hu, F. Ren, H. Ding, Y. Fu, and B. Tan, "Study on the process and mechanism of slope failure induced by mining under open pit slope: a case study from yanqianshan iron mine, China," *Advances in Civil Engineering*, Article ID 6862936, 26 pages, 2019.

[12] Z. Wang, Y. Tian, W. Zhou, Z. Liu, X. Lu, and R. Kong, "Steep end-slope mining and slope stability of extremely thick inclined coal seam open-pit mine," *Mathematical Problems in Engineering*, vol. 2022, Article ID 3807013, 9 pages, 2022.

[13] H. Wang, B. Zhang, G. Mei, and N. Xu, "A statistics-based discrete element modeling method coupled with the strength reduction method for the stability analysis of jointed rock slopes," *Engineering Geology*, vol. 264, Article ID 105247, 2020.

[14] Q. X. Meng, H. L. Wang, W. Y. Xu, M. Cai, J. Xu, and Q. Zhang, "Multiscale strength reduction method for heterogeneous slope using hierarchical FEM/DEM modeling," *Computers and Geotechnics*, vol. 115, Article ID 103164, 2019.

[15] Z. H. Zhou, Z. H. Chen, M. Bao, Q. G. Nian, and W. Zhang, "Stability of rock slope with bedding intermittent joints based on catastrophe theory," *Journal of China Coal Society*, vol. 45, pp. 161–172, 2020.

[16] M. J. Jiang, T. Jiang, G. B. Crosta, Z. M. Shi, H. Chen, and N. Zhang, "Modeling failure of jointed rock slope with two main joint sets using a novel DEM bond contact model," *Engineering Geology*, vol. 193, pp. 79–96, 2015.

[17] L. Scholtès and F. V. Donzé, "A DEM analysis of step-path failure in jointed rock slopes," *Comptes Rendus Mecanique*, vol. 343, no. 2, pp. 155–165, 2015.

[18] H. B. Wang, B. Zhang, G. Mei, and N. X. Xu, "A statistics-based discrete element modeling method coupled with the strength reduction method for the stability analysis of jointed rock slopes," *Engineering Geology*, vol. 264, Article ID 105247, 2019.

[19] K. Zhao, Y. W. Zeng, and C. Zeng, "Stability analysis of rock slope with weak structural surface based on particle flow method," *Science Technology and Engineering*, vol. 18, pp. 97–102, 2018.

[20] M. B. Victor and K. Tedius, "Wedge Failure Analyses of the Jointed Rock Slope Influenced by Foliations," *Geotechnical and Geological Engineering*, vol. 38, 2020.

[21] Z. Li, Z. Hu, W. L. Liu, G. J. Hu, S. G. Du, and Y. Zhou, "Plastic limit analysis of open-pit mine jointed rock slope considering

translation-rotation mechanisms," *Chinese Journal of Rock Mechanics and Engineering*, vol. 37, pp. 4056–4068, 2018.

[22] Y. C. Song and X. S. Sun, "Stability analysis of rock slope with connected joint," *Rock and Soil Mechanics*, vol. 35, pp. 365–372, 2014.

[23] Q. Shen, C. X. Chen, and R. Wang, "Study on stability of horizontal bedded rocky slopes in Three Gorges Reservoir area," *Rock and Soil Mechanics*, vol. 26, pp. 16–20, 2005.

[24] E. Z. Lajtai, "Brittle fracture in compression," *International Journal of Fracture*, vol. 10, no. 4, pp. 525–536, 1974.

[25] A. Bobet and H. H. Einstein, "Fracture coalescence in rock-type materials under uniaxial and biaxial compression," *International Journal of Rock Mechanics and Mining Sciences*, vol. 35, no. 7, pp. 863–888, 1998.

[26] B. Yuan, Z. Li, W. Chen et al., "Influence of groundwater depth on pile–soil mechanical properties and fractal characteristics under cyclic loading," *Fractal and Fractional*, vol. 6, no. 4, p. 198, 2022.

[27] M. Ma, M. Li, X. Qu, and H. Zhang, "Effect of passing metro trains on uncertainty of vibration source intensity: monitoring tests," *Measurement*, vol. 193, Article ID 110992, 2022.

[28] B. Bai and T. Li, "Irreversible consolidation problem of a saturated porothermoelastic spherical body with a spherical cavity," *Applied Mathematical Modelling*, vol. 37, no. 4, pp. 1973–1982, 2013.

[29] C. Zou, J. A. Moore, M. Sanayei, Z. Tao, and Y. Wang, "Impedance model of train-induced vibration transmission across a transfer structure into an over track building in a metro depot," *Journal of Structural Engineering*, vol. 172, 2022.

[30] Y. Liu, D. Zhang, S. Wu, and P. Yu, "DEM investigation on the evolution of fabric under true triaxial conditions in granular materials," *International Journal of Geomechanics*, vol. 20, no. 8, Article ID 04020110, 2020.

[31] X. S. Li and Y. F. Dafalias, "Anisotropic critical state theory: role of fabric," *Journal of Engineering Mechanics*, vol. 138, no. 3, pp. 263–275, 2012.

[32] B. Bai, Y. Wang, D. Rao, and F. Bai, "The effective thermal conductivity of unsaturated porous media deduced by pore-scale SPH simulation," *Frontiers of Earth Science*, vol. 10, 2022.

[33] C. S. Chang and P. Y. Hicher, "An elasto-plastic model for granular materials with microstructural consideration," *International Journal of Solids and Structures*, vol. 42, no. 14, pp. 4258–4277, 2005.

[34] X. Gu, X. Liang, Y. Shan, X. Huang, and A. Tessari, "Discrete element modeling of shear wave propagation using bender elements in confined granular materials of different grain sizes," *Computers and Geotechnics*, vol. 125, Article ID 103672, 2020.

[35] H. Jin, Q. Tian, and Z. Li, "Crack development of rebar rust in rubberized concrete using mesoscale model," *Construction and Building Materials*, vol. 321, Article ID 126409, 2022.

[36] B. Bai, R. Zhou, G. Cai, W. Hu, and G. Yang, "Coupled thermo-hydro-mechanical mechanism in view of the soil particle rearrangement of granular thermodynamics," *Computers and Geotechnics*, vol. 137, no. 8, Article ID 104272, 2021.

[37] H. Jin, J. Su, and C. Zhao, "Relationship between invert-filling disengaging and deformation of shield tunnel using staggered assembled segment," *KSCE Journal of Civil Engineering*, vol. 26, no. 4, pp. 1966–1977, 2022.

[38] D. O. Potyondy and P. A. Cundall, "A bonded-particle model for rock," *International Journal of Rock Mechanics and Mining Sciences*, vol. 41, no. 8, pp. 1329–1364, 2004.

[39] L. Xu and M. Ma, "Dynamic response of the multilayered half-space medium due to the spatially periodic harmonic moving load," *Soil Dynamics and Earthquake Engineering*, vol. 157, Article ID 107246, 2022.

[40] X. Wang, Y. Liu, and P. Yu, "Upscaling critical state considering the distribution of meso-structures in granular materials," *International Journal for Numerical and Analytical Methods in Geomechanics*, vol. 45, no. 11, pp. 1624–1646, 2021.